Nonreciprocal GHz surface acoustic wave behavior based on phononic crystal heterojunction: Numerical study

Rahman Sharaf[1], Sara Darbari[1*], Abdelkrim Khelif[2]

[1] *Nano Sensors and Detectors Laboratory, Nano Plasmophotonic Research Group, Faculty of Electrical and Computer Engineering, Tarbiat Modares University, Tehran 1411713116, Iran*

[2] *FEMTO-ST Institute, UBFC, CNRS, ENSMM, UTBM, 15B Avenue des Montboucons, 25030 Besançon, France*

* Corresponding Author: s.darbari@modares.ac.ir

Abstract: In this report, a rectifying SAW device is proposed and simulated based on a simple static phononic crystal (PnC) heterojunction, consisting of monolithic pillars on Si substrate for the first time. The designed nonreciprocal operation principle is initially based on the frequency alignment of the surface coupled guiding bands in the first half PnC with the local surface resonance (LSR) bandgap in the second half PnC. Benefiting from the flexible bandgap engineering in LSR bandgaps, we have tuned the bandgap central frequency in miniature dimensions by optimizing the structural dimensions of the pillars, which is not achievable in conventional Bragg bandgaps without varying the lattice constant. The other principle to amplify the broken reciprocal behavior in our design is based on the polarization conversion of SAW from shear to sagittal, depending on the incident direction in one the half PnCs. Moreover, we have changed the spacing gap between the PnCs to modulate the elastic coupling strength between the half PnCs, and optimized the nonreciprocal transmission behavior. We have proved a significant nonreciprocity of 34 dB in the SAW transmission at the frequency of 6.9 GHz, beside an acceptable rectified transmission of about -10.68 dB. The proposed design benefits from a monolithic Si-based structure and simple fabrication process, without the need for any external excitation, and it can be entitled as a promising miniature and efficient SAW rectifying candidate for wireless communication applications.

Keywords: Surface acoustic wave; phononic crystal; nonreciprocity; local surface resonance

I. INTRODUCTION

Nonreciprocity is defined as breaking the symmetry in the forward and backward transmissions of a system in response to different incident wave directions [1]. Rectifiers, isolators, and circulators are different type of nonreciprocal devices that have found many applications in electromagnetics, acoustics, and elastic fields [2-5]. There are many interests in nonreciprocal structures at microwave frequencies beyond 100 MHz for controlling wave propagation in radio frequency communications, quantum technology systems, and on-chip processing applications [6-9]. However, realizing a magnetic-free nonreciprocal behavior and CMOS-compatible fabrication technology have been mostly challenging and desirable issues [6].

Introducing surface acoustic wave (SAW) devices proposed the potential to use elastic waves instead of electromagnetic waves in radar receivers to replace the bulky devices (mm~m) with micrometer counterparts, because of the lower speed of elastic phonons, which is five orders of magnitude less than that of a photon [10]. SAW devices have been found attractive for a wide range of applications [11], such as on-chip RF filters, an impartible component in wireless communications [12], microfluidics [13], different kinds of sensors [14], [15], hybrid quantum technologies [16], acousto-optic and acoustoelectric devices [17-19]. Benefiting from SAW devices, elastic nonreciprocity has been practical for frequency range from few hundreds of MHz to several GHz; wherein low loss devices with micrometer and sub-micrometer dimensions are feasible [20]. Some recent reports on elastic nonreciprocity use external excitations to change the material/elastic wave coupling in the delay line through magnetoelastic and acoustoelectric effects [5,7,20,21]. Other recently proposed designs include hybrid schemes that use switching networks in conjunction with SAWs delay lines [9], or parity-time symmetric nonlinear system [6].

Solid phononic crystals (PnCs), as the elastic counterparts of photonic crystals, are periodic arrangement of elastic scatterers in a host matrix, and have shown application in different fields such as filters [22], demultiplexers [18,23], sensors [24], heat transfer [25], energy harvesting [26,27] and resonators [28]. PnCs, consisting of periodic pillars on the substrate, can lead to local surface resonance (LSR) bandgaps for elastic surface coupled modes, as compared with the hole-based PnCs in which only Bragg reflections are responsible for emerging the bandgaps [29]. The central frequency of the Bragg bandgaps is proportional to the lattice constant inversely, wherein the reflection and

transmission of the PnC are maximized and minimized, respectively. However, LSR modes originate from hybridization of the individual resonances of the scatterers with the surface elastic modes, which may lead to open low-frequency LSR bandgaps. Moreover, LSR modes show generally slower propagation velocity in comparison with the surface modes of the bare substrate, because the elastic energy is delayed by local resonances in the scatterers [30].

In this report, a monolithic Si-based nonreciprocal SAW device is designed and simulated, which benefits from two different PnCs with a heterojunction in the delay line. Taking advantage of resonating pillars in the PnC and the LSR bandgaps, we present a miniature device with high SAW nonreciprocity in GHz frequency range, without the need for any external excitation fields [5,7,20,21], wave bending [31], or rotation of a half PnC with respect to the other half [4]. The proposed elastic rectifier is a simple, CMOS-compatible, magnetic-free and efficient candidate for on-chip GHz processing, proposing promising output characteristics as compared with the previous reports [5,20,21].

II. THEORY AND IMPLEMENTATION OF SIMULATION

The proposed nonreciprocal SAW structure is composed on two phononic crystals with a heterojunction, each of which made of Si pillars on Si substrate. The achieved optimized nonreciprocal behavior is designed initially based on the band structure. Therefore, we present the band structures of the PnCs, especially the surface coupled bands and the relating elastic modes. For this purpose, we consider a unit cell of the PnC with periodic boundary conditions (PBCs) on all four side walls, according to Fig. 1(a). It can be observed that the unit cell consists of the substrate and a cylindrical pillar on top of it. Moreover, to calculate the transmission spectra of the proposed PnCs along *x* direction, we consider a supercell with 10 pillars along the wave propagation direction with PBCs on the lateral side walls (along ±*y* directions), as shown in Fig. 1(b). Equations (1) and (2) are the coupled equations for solving the propagation of the elastic waves [22]:

$$S_{ij} = \frac{1}{2}(\partial_j u_i + \partial_i u_j) \quad \textbf{(1)}$$

$$T_{ij} = C_{ij} S_{ij} \quad \textbf{(2)}$$

Wherein S_{ij}, T_{ij}, $u_{i,j}$, and C_{ij} are the strains, the mechanical stresses, the atomic displacements, and the elastic stiffness components along $i,j=x,y,z$ directions. It

should be noted that PBC follows the Bloch-Floquet theorem for the elastic waves, so that [32]:

$$u_i(x+a, y+a) = u_i(x,y)e^{-i(k_x a + k_y a)} \quad \textbf{(3)}$$

Wherein k_x and k_y are the Bloch wave vectors. For boundaries along +z direction we have assumed free surface condition, while along –z direction we have assumed fixed and low reflection boundaries in figures 1(a) and 1(b), respectively. Moreover, for the front and back sides (±x directions) of the supercell in Fig. 1(b), we have assumed damping layers to minimize the wave reflections from these boundaries.

Structural parameters of the investigated PnCs are shown in Fig. 1(a), in which r, h_p, a, and h_s represent the pillar radius, pillar height, lattice constant, and the substrate thickness, respectively. It is notable that to achieve the desired nonreciprocal behavior for SAWs in GHz frequency range, we have used two different lattice constants of a=100, and 200 nm, while assuming a fixed h_p=100 nm. Concerning that SAWs are confined to the surface and penetrate to a depth of about one wavelength from the top surface of the substrate [33], we have assumed a substrate thickness, five times greater than the larger lattice constant (h_s=1μm) to decouple the surface waves from Lamb waves [32]. Finally, considering the crystalline symmetry of Si, we have three independent anisotropic elastic constants of C_{11}=165.7 GPa, C_{12}=63.9 GPa, and C_{44}=79.9, and the mass density of ρ=2331 kg/m^3 for the investigated PnCs [32].

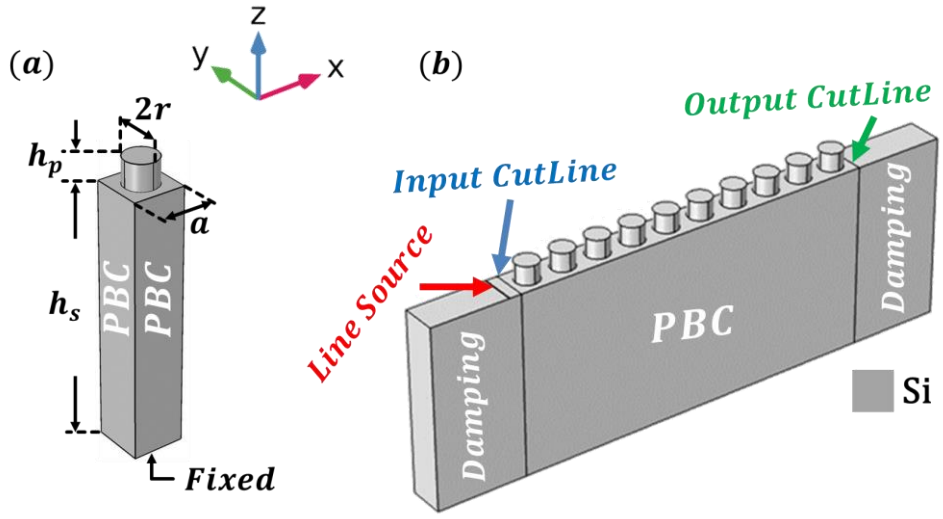

FIG. 1. (a) The unit cell of the PnC, used for calculating the relating band structure. (b) The supercell of the PnC with 10 rows of pillars along the wave

propagation direction, used for calculating the transmission spectrum.

As shown in Fig. 1(b), a line source along *y* direction is used at the top surface of the super cell in order to excite the incident SAWs mechanically. Moreover, the input and output cut-lines are shown on the surface, along which the integral of the input and the output elastic energies are calculated by Eq. (4). Transmission value is achieved from the ratio of the calculated output to input elastic energies.

$$T = u_x^2 + u_y^2 + u_z^2 \quad \textbf{(4)}$$

To investigate the transmission behavior of the proposed structure, we should consider two polarizations:

1. The sagittal polarized surface source with displacement components of u_x and u_z (in *xz* plane), which leads to excitation of Rayleigh SAWs.
2. The shear polarized source in y direction with displacement component of u_y (in *y* direction), which leads to excitation of shear horizontal SAWs.

All simulations for numerical calculations of the band structures and the transmissions are fulfilled by using the finite element method (FEM).

III. THE BASIC OPERATINAL BEHAVIOR

Figures 2(a) and (b) show the achieved band structures in the first Brillouin zone of PnCs with pillar radii and lattice constants of r_L=40 nm, a_L=100 nm for the left PnC, and r_L=85 nm, a_R=200 nm for the right one. The inset in part (b) shows the first Brillouin zone for the square lattice of both PnCs. The dark blue regions in the band structures cover the bulk modes, while the lower frequency colored bands in the white background show the surface bands. The interface between the dark blue and white region is the sonic cone, which is the boundary between the bulk and surface bands. In other words, the sonic cone represents the bulk modes with the minimum group velocities, thus separates the bulk modes from the surface modes with lower velocities. Moreover, we have presented the sagittal to shear polarization ratio of the surface modes at each wave vector by the band color. This ratio is calculated by dividing the maximum sagittal displacement component to that of the shear displacement ($\max(u_z,u_x)/\max(u_y)$) for each point in the band structure. Furthermore, the surface bands of the bare substrate are calculated and superimposed in both band structures of Fig. 2(a) and 2(b), which are shown by dashed colored bands. To calculate the surface bands of the bare substrate, we have removed the pillars

from the unit cell in Fig. 1(a) and calculated the band structure. It is observable in these figures that the first substrate's surface band is sagittal polarized in Γ*X* direction. Moreover, it can be observed that the surface coupled bands in theses PnCs have a lower slope than those of the surface modes in bare substrate, which means that the surface elastic waves are slowed down at the presence of pillars, as the local resonators. This observation is attributed to creation of the surface coupled modes or LSR modes for these PnCs, in which the resonating pillars are coupled to the substrate surface. Partial local resonance of the surface wave in the pillars is the main reason of the observed reduced wave velocity for the PnCs. Fig. 2(c) displays the displacement profile at some selected modes (points A to E) in Fig. 2(b). In this figure, points A and D are related to the first and the third surface coupled modes at *X* and *M* points with frequencies of 6 and 10.5 GHz, respectively. Point B (C) is related to the second (first) surface band of the PnC (bare substrate) at frequency of 6.8 GHz, while point E demonstrates a bulk mode at 16 GHz to elaborate the difference between the displacements of surface and bulk modes. The total displacements (u) relating to these points are shown in Fig. 2(c), wherein the surface coupled elastic modes of the PnC at A, B, and D are mostly confined to the pillars and shows a very shallow penetration in the substrate. However, for the bulk mode at E the elastic mode is delocalized and the displacement profile is distributed both in the pillar and the whole substrate thickness of the unit cell. On the other hand, for the pillar-less substrate at point C, the surface mode is confined at about the top 200 nm thickness of the substrate, but the penetration depth of the surface mode is absolutely larger than that of the surface coupled modes (A, B, D). This figure manifests the difference between the surface coupled modes at the presence of local resonators (pillars), and the pure surface modes when the top pillars are absent. Moreover, the displacement components for points B and C are shown along *x* (u_x), *y* (u_y), and *z* (u_z) directions in Fig. 2(d) and 2(e), respectively (at 6.8 GHz). As shown in Fig. 2(d), for the second surface coupled band at B, u_y and u_z are dominant components, and this mode is considered as a shear polarized mode, the fact that we have represented by the blue color of the band at this point, according to the color bar. Fig. 2(e) illustrates the displacement components of the first surface band of the substrate at C, revealing that sagittal components (u_x and u_z) are dominant as compared with the *y*-component of displacement, which is represented by the red color of the dashed band at point C. To elaborate the polarization behavior of the surface coupled modes in PnCs, for instance at mode B in Fig. 2(b) we can determine a sagittal to shear ratio of

0.48 from the color bar, which is in agreement with the presented $max(u_z)/max(u_y)$ ratio in Fig. 2(d), and means that the shear polarization is dominant at this point. As shown in Fig. 2(a) and (b), the first and the second surface coupled bands in Γ*X* direction of the PnC are overall sagittal and shear bands, respectively. Moreover, it can be observed that as the slope of the band increase/decrease, the mode polarization coverts into sagittal/shear. The other worthy observation is that when two surface bands approach to each other, similar to the 3th and the 4th bands along Γ*X* direction in Fig. 2(a) and along *XM* direction in Fig. 2(b), a polarization exchange occurs between the bands.

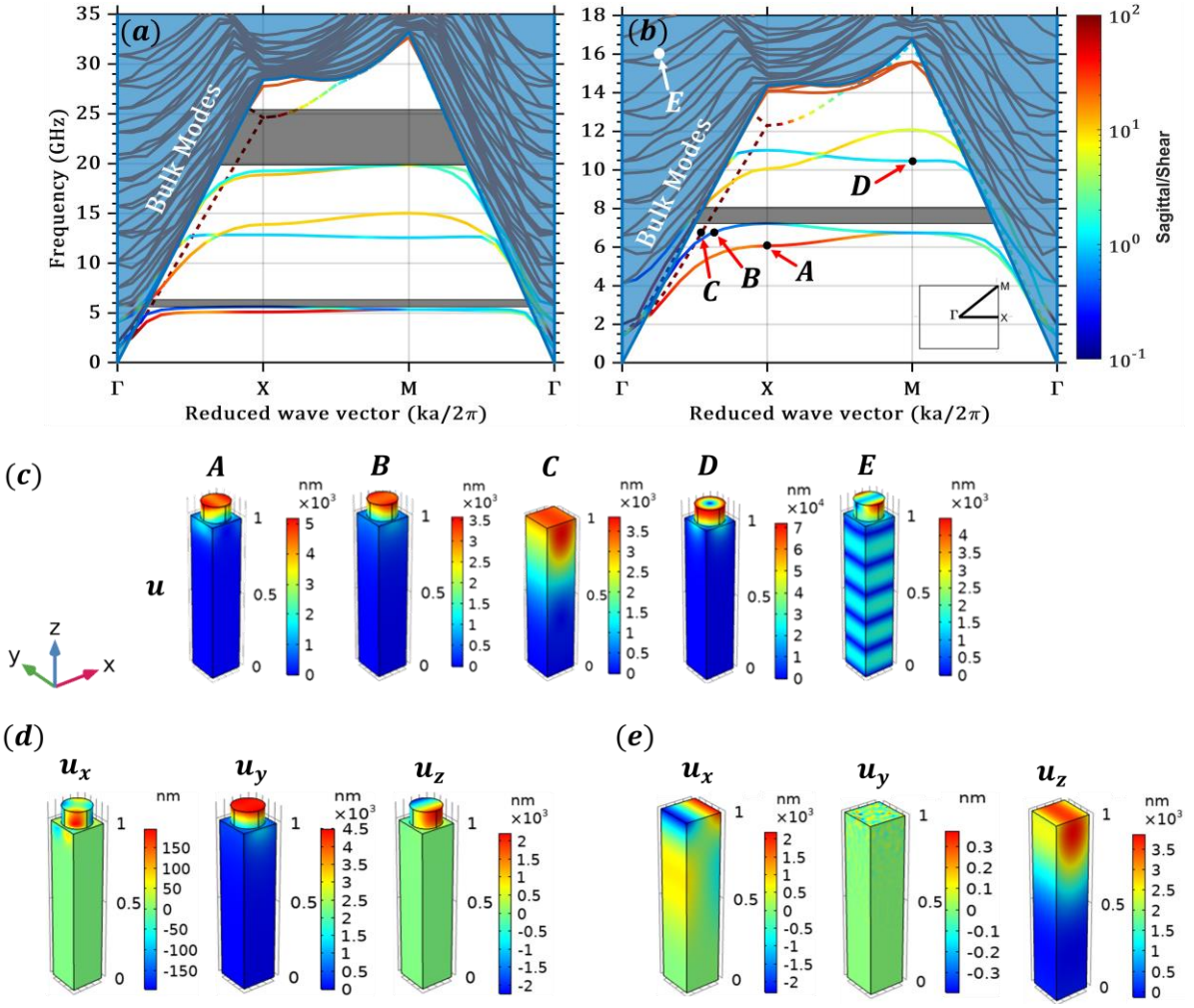

FIG. 2. The calculated band structure for the unit cell with: (a) r_L=40 nm and a_L=*100 nm*, and (b) r_R=85 nm and a_R=200 nm. The inset in part (b) shows the first irreducible Brillouin zone of the square lattice. The dashed bands in both band structures show the surface bands of the bare substrate. (c) The profiles of the total displacements (*u*) for points A, B, C and D in part (b). Displacement components along *x* (u_x), *y* (u_y) and *z* (u_z) directions for: (d) point B, and (e)

point C.

Considering the presented band structures in Fig. 2(a) and (b), we expect different transmission spectra for the investigated PnCs at different directions. Therefore, a nonreciprocal transmission behavior can be achieved by engineering the PnCs structures, and the relating band structures. For example, in Fig. 2(a) there are surface coupled bands both in Γ*X* and *M*Γ directions at frequency of 12 GHz, while in Fig. 2(b) transmission is forbidden at this frequency because surface bands are absent in Γ*X* direction. Moreover, two surface bandgaps are observed in Fig. 2(a) with gap center frequencies of 6 and 22.5 GHz, which are shown by gray bars. The lower frequency gap is a LSR bandgap between the surface coupled bands, which in turn are originated from the elastic coupling between discrete resonances of pillars and the surface modes of the substrate. LSR bandgaps are strongly depending on the structural properties of pillars, such as height and radius, while do not change significantly by changing the lattice constant. The upper gray bandgap in Fig. 2(a) is dominantly a Bragg gap with a central gap frequency (f_c), which is determined by the SAW velocity (v) and the lattice constant (a) of the PnC through the relation of $f_c \approx v/2a$. Similarly, we have investigated the band structure in Fig. 2(b), in which one LSR bandgap is observed at 7.5 GHz (shown by a gray bar). Then, we investigate the transmission spectra for the sagittal and shear polarized sources, using the illustrated super cell in Fig. 1(b). Figure 3 shows the reduced band structures in Γ*X* direction beside the calculated transmissions for the PnCs with r_L=40 nm, a_L=100 nm in part (a), and r_R=85 nm, a_R=200 nm in part (b). We have illustrated the partial band gaps in the presented reduced band structures by gray bars. It is observable that the achieved transmissions are in agreement with the previously discussed band structures and displacement polarizations in figures 2(a) and 2(b). Moreover, it can be observed in Fig. 3 that Bragg bandgaps in part (a) are broader than those of part (b), while the opposite behavior is observed for LSR bandgaps in these two parts of the figure. This observation is in accordance with the Bragg and LSR gaps in the band structures of Fig. 3(a) and 3(b). The other worthy observation is that the shear transmissions show deeper LSR bandgaps with lower transmission values, as compared with the sagittal transmissions. We believe that the negligible *x*-component of the shear modes along wave propagation (*x*-direction) leads to a weaker elastic coupling between the pillars, making the shear wave propagation slower and the shear bands flatter (less dispersive) in comparison with the

sagittal bands. The flatter shear bands, as the upper and lower extremes of the LSR band gap in shear transmissions are the main reason for achieving deeper shear gaps with lower transmission values. These deep LSR gaps in shear transmissions can be beneficial to achieve a higher nonreciprocal transmission behavior in our designed PnC structure. Therefore, we focus on shear waves in the rest of simulation results in this paper.

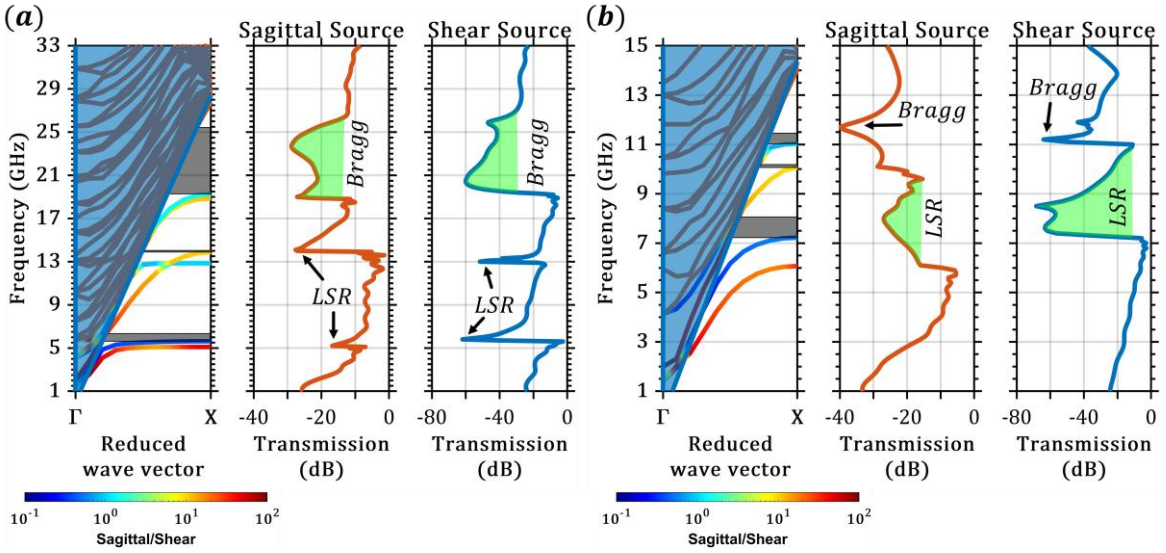

FIG. 3. The calculated reduced band structures, besides the sagittal and shear transmission spectra for the PnCs with (a) r_L=40 nm and a_L=100 nm, and (b) r_R=85 nm and a_R=200 nm.

To validate our latter discussion about the elastic coupling between the pillars of PnCs in shear and sagittal modes, we have presented the elastic energy distribution for the shear and sagittal wave propagations at the central frequency of their relating LSR gap. Figure 4(a) shows the 3D profile of the elastic energy for shear and sagittal excitations, within a supercell of r_L/a_L=40/100 (nm/nm) at 6 GHz, while Fig. 4(b) displays the elastic energy profile for r_R/a_R=85/200 (nm/nm) at f=7.5 GHz. For more clearance, in parts (c) and (d) we have presented the 2D top views of the energy distribution for shear and sagittal modes of the investigated PnCs at the substrate's surface, corresponding to parts (a) and (b) of Fig. 4. It is known that the resonating pillars in the PnC are elastically coupled to each other through the top surface of the substrate. Thus, higher elastic energy at the substrate surface between the neighboring pillars reveals higher elastic coupling between the pillars, which leads to more dispersive surface coupled bands and higher wave velocity consequently. As

can be observed in Fig. 4(c) and 4(d), for the shear excitation the energy coupling between the pillars in x direction is weaker than the sagittal one. Moreover, the energy is mostly confined in the pillars, as compared with the substrate surface in shear modes, however, both pillars and substrate surface are involved in the energy distribution of sagittal modes. Hence, we can definitely attribute the observed deeper LSR gaps in shear modes to the proved weaker elastic coupling between the resonating pillars. In contrary, as the elastic coupling between the neighboring pillars in the PnC increases in sagittal excitation, the sagittal LSR bandgap transmission value increases consequently.

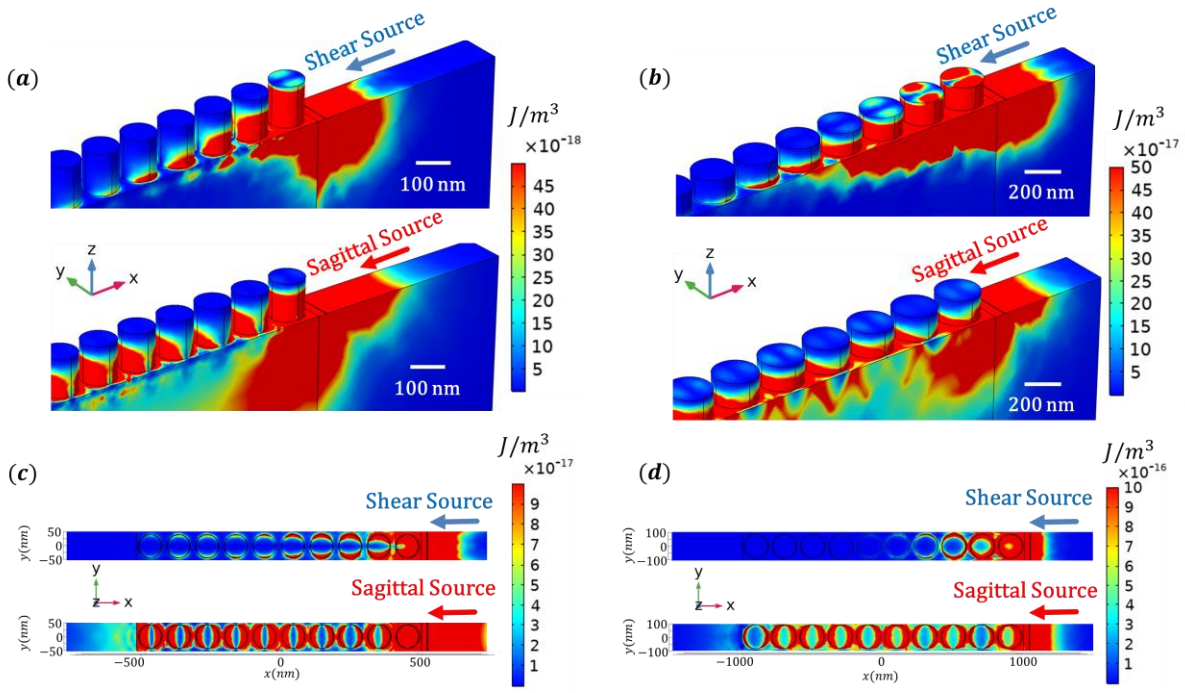

FIG. 4. The profile of the stored elastic energy in the super cells with (a, c) r_L/a_L=40/100 (nm/nm) at 6 GHz, and (b, d) r_R/a_R=85/200 (nm/nm) at 7.5 GHz. (a) and (b) show the 3D view, while (c) and (d) show the top view of the elastic energy distribution for the shear and sagittal sources.

IV. THE PROPOSED DEVICE STRUCTURE, NUMERICAL RESULTS AND DISCUSSION

Figure 5(a) shows the proposed structure with nonreciprocal SAW behavior, which consists of a heterojunction between two PnCs. The structural parameters of the right PnC, including the pillar radius and the lattice constant are r_R=85 nm, and a_R=200 nm, while those are r_L=40 nm and a_L=100 nm for the left PnC.

Both left and right PnCs have square lattice with a Γ*M* heterojunction between them. Moreover, we have assumed an interspacing gap of *d* along *x*-direction between two adjacent unit cellsof the neighboring PnCs at the heterojunction. Damping conditions are considered for all boundary layers along the *x* and *y* directions to avoid reflections, and free surface and low reflection boundary conditions are assumed for the top (+*z*) and bottom (-*z*) surfaces of the device, respectively. N_{ext} is the number of pillars of the right PnC edge, extended away from the interface. Considering $a_R=2a_L$ in the proposed structure, we have assumed the number of extended pillars in the left PnC edge equal to $2N_{ext}$, in order to achieve a symmetric structure.

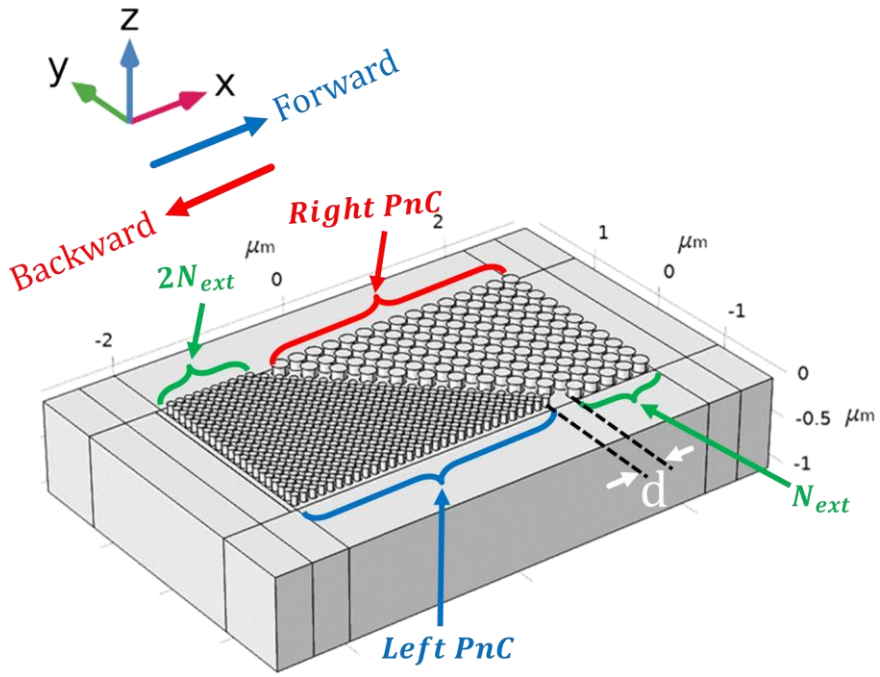

FIG. 5. The proposed nonreciprocal device consists of two PnCs: the right PnC with r_R=85 nm and a_R=200 nm, and the left PnC with r_L=40 nm and a_L=100 nm. Two PnCs are cut at 45° and joint with an interspacing gap of *d*. The forward excitation is along +*x* and the backward one is along -*x* direction, as shown in the figure.

To study the transmission behavior of the proposed nonreciprocal structure, first we investigate the right and left PnCs separately. In this regard, Fig. 6(a) shows the individual right PnC schematially, wherein green lines demonstrate the forward and backward input cultlines along +*x* and -*x* directions, respectively. To evaluate the forward and backward transmission spectra we

calculate the transmitted elastic energies through Eq. (4). Our simulation results showed that for the pillar numbers larger than 11 along *y* direction, reflections from the up and down boundary edges of the PnC, along the *x* direction, are negligible, and do not change significantly by increasing the pillars number. Therefore, we have assumed 11 pillars along the right boundary (along *y* direction) of the right PnC to save simulation time consumption. It should be noted that the forward incident direction (blue arrows in part (a)) corresponds to the *M*Γ incident direction, and the backward incident direction (red arrows in part (a)) corresponds to the Γ*X* incident direction with respect to the illustrated PnC structure. Figure 6(b) indicates the reduced band structure of the right PnC along *M*Γ and Γ*X* directions, wherein the partial bandgaps are shown by yellow and cyan bars, respectively. Here, solid colored bands are the surface coupled bands of the PnC, and the dashed band shows the surface band of the bare substrate. The black horizontal line highlights the specific frequency of 6.8 GHz in the band structures, which corresponds to a surface coupled shear band in the backward excitation (Γ*X* direction). However, in the forward excitation (*M*Γ direction) this frequency lies in the low frequency LSR bandgap (bottom yellow gap). Considering this observation in the bandstructure, we expect a nonreciprocal behavior for SAWs at f=6.8 GHz, because the wave transmission is forbidden in the forward direction, while it is allowed to propagate through the PnC in the backward direction. Then, to elaborate the wave propagation, in Fig. 6(c) we plot the iso-frequency contours in a unitcell of this PnC, which are calculated from the intersection of constant frequency planes with the dispersion surface of a specific mode in the band stucture of Fig. 6(b). It is evidently observable here that contours relating to f=6.8 GHz show anisotropic behavior with respect to the wave vector direction, so that they cross with the incident wavevectors of k_y=0, while they do not cross with the incident wavevectors of k_x=k_y. This observation reveals the inherent non-reciprocal transmission behavior of the investigated individual right PnC in response to SAWs. As can be seen in the bandstructure (part (b)) frequencies below about 4 GHz lead to bulk modes (dark blue region), and do not correspond to any surface bands. Cyan region in the iso-frequency plot represents the bulk modes of the PnC relating to frequencies below about 4 GHz. Moreover, if we increase the input frequency from 6.8 GHz to about 7.2 GHz, we have allowed bands in the backward direction (in the Γ*X* direction); in contrary, we go deeper in the LSR gap of the forward direction (yellow gap in the *M*Γ direction). This behavior in the bandstructure is reflected in the iso-frequency contours by shrinkage of iso-

frequency contours towards k_y=0 and pure k_x values, so that incident wavevectors with $k_y \neq 0$ do not cross with those iso-frequency contours. In other words, incident wavevectors along $M\Gamma$ direction become completely forbidden. Regarding a similar trend, input frequencies higher than about 7.2 GHz do not correspond to any surface coupled bands in the bandstructure of both $M\Gamma$ and ΓX directions (part (b)), which coressponds to disappearence of the allowed iso-frequency contours in Fig. 6(c).

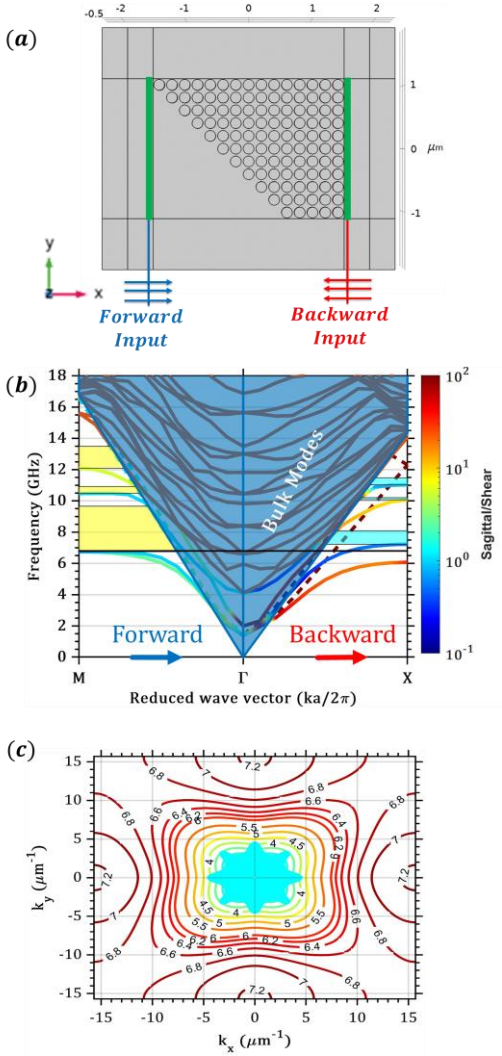

FIG. 6. (a) The scheme of the individual right PnC. (b) The calculated band structure for the right PnC, and (c) the iso-frequency contours around the second surface coupled band.

Shear forward/backward transmission spectra of the right PnC are demonstrated in Fig. 7(a). Here, the exerted input source is assumed shear polarized, while all the displacement components at the output are cosidered for the transmission calculations. In this figure, we observe that backward transmission value is about 16 dB higher than the forward transmission value at

input frequency of 6.8 GHz, which reveals the maximum nonreciprocal behavior of the right PnC. Moreover, the backward transmission value at this nonreciprocal frequency is -11 dB, while the forward transmission is approximately forbidden. Then, to elaborate the backward transmission behavior, we demonstrate the decoupled sagittal ($u_x^2+u_z^2$) and shear (u_y^2) components of the backward transmission, beside the total backward transmission in Fig. 7(b), wherein the proposed nonreciprocal frequency is highlighted by a vertical black line. It can be observed that a polarization conversion phenomenon occurs at the nonreciprocal frequency. In other words, the incident backward shear polarized excitation converts to a pure sagittal polarized elastic wave, so that the sagittal component is about 30 dB higher than that of the shear component of the backward transmission. This polarization conversion is attributed to the strong coupling between the shear polarized surface coupled mode of the PnC (solid band), and the sagittal polarized substrate surface mode (dashed band), observed at frequency of 6.8 GHz in the Γ*X* direction of the relating bandstructures in Fig. 2(b) and 6(b). In other words, the particular geometrical parameters of the right PnCs are such that both surface coupled mode, hybridized between the pillars and the substrate, and the pure substrate surface mode occur nearly at the same frequency of 6.8 GHz. According to the mode displacement components of points B and C (in Fig. 2(b)), shown in Fig. 2(d) and 2(e), the second surface coupled band of the right PnC supports u_y and u_z components, while the bare substrate supports surface modes with u_x and u_z components. Hence, the coupling between the latter two modes implies that only u_z resonances can be transmitted through the PnC, or equally the strongest displacement component is the *z* component.

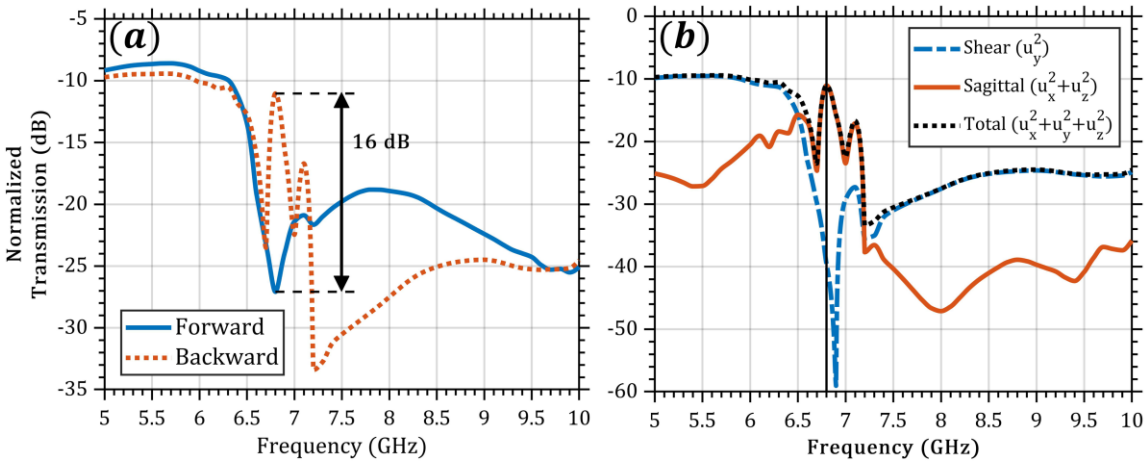

FIG. 7. (a) Normalized transmission spectra for the forward (+*x*) and

backward (-*x*) shear inputs. (b) Components of the backward transmission in part (a), separated in the shear (u_y^2) and sagittal ($u_x^2+u_z^2$) components.

Figures 8(a) and (b) display the total displacement profiles for the forward and backward propagation directions of the investigated right PnC. As it is observable, the forward and backward elastic waves pass through the PnC, mostly along the *x* direction, while the reflections from the ±*y* boundaries are negligible. For more clarification, we demonstrate the forward displacement profile in a *xz* cut plane at the middle of the PnC structure, as shown in Fig. 8(c). In the presented bulk cross section, we can observe that most of the forward incident wave is coupled to the bulk, and surface coupled wave is attenuated significantly so that leads to a very low transmision value at the surficial output cutline. This bulk coupled forward propagation results in the observed nonreciprocal behavior for SAWs. To elaborate the transmission behavior of the right PnC, we present the 2D displacement distributions in *xz* plane for the forward and backward shear excitations at excitation frequencies, corresponding to reciprical and nonreciprocal frequencies, as shown in Fig. 9. For this purpose, we have chosen frequencies of 5 GHz (parts a,b), 6.8 GHz (parts c,d), and 11 GHz (parts e,f), in turn corresponding to the reciprocal, nonreciprocal, and reciprocal behaviors, according to Fig. 7(a). As Fig. 9 indicates, the forward (upper profiles) and backward displacement distributions (bottom profiles) lead to high surficial displacements at the output cutlines for the reciprocal frequencies of 5 and 11 GHz. However, for frequency of 6.8 GHz, the surfacial output displacement is negligible in forward excitation, as opposed with the backward excitation. This strong asymetric displacement profiles in the forward and backward excitations reveals the nonreciprical behavior of the proposed PnC for SAWs. Moreover, the displacement profiles in Fig. 9 clarify the coupling between the pillars and the substrate surface for the allowed transmissions. However, the surface wave transmission is significantly attenuated when the coupling between the pillars and the surface is weakened, as shown in the forward excitation at f=6.8 GHz. The other worthy point is that surface coupled modes are completely emerged in both the forward and backward directions for f=5 GHz, so that both forward and backward transmissions are high. However, for f=11 GHz, surface coupled waves are disturbed, so that despite of the reciprocal transmission, we observe low forward and backward transmissions.

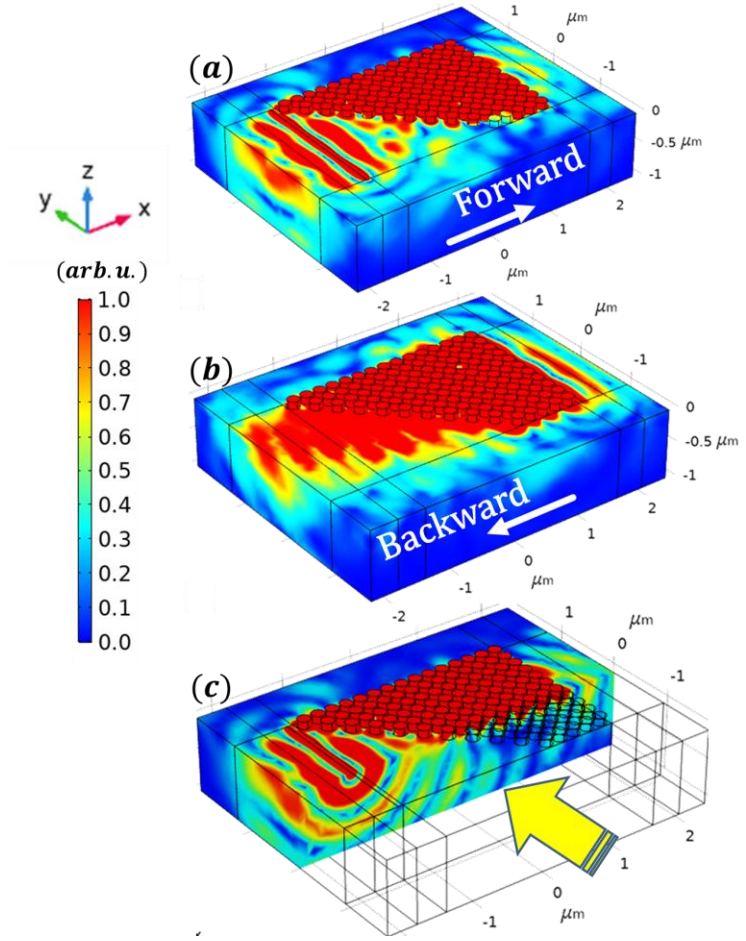

FIG. 8. Total displacement distribution at 6.8 GHz for the right PnC for (a) the forward and (b) the backward transmissions. (c) The profile of the total displacement in the *xz* cross section.

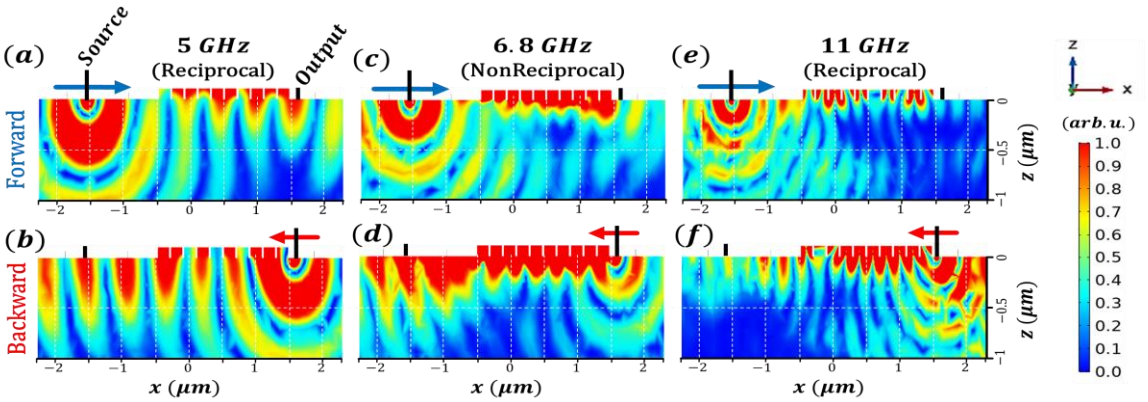

FIG. 9. Total displacement profiles of the right PnC in *xz* plane for the forward and backward incident directions at the frequency of (a, b) 5 GHz, (c, d) 6.8

GHz, and (e, f) 11 GHz.

As the next step, we have performed a similar studying procedure to evaluate the individual behavior of the left PnC in the proposed device structure (Fig. 5). Figures 10(a) and 10(b) show the individual left PnC and the corresponding band structure, respectively. Here, the forward direction in part (a) corresponds to the Γ*X* direction, while the backward direction corresponds to the *M*Γ direction in the PnC (as shown in the band structure of part (b)). Again, the dashed bands in the bandstructure of Fig. 10(b) show the first and second surface bands of the bare substrate. Two solid black horizontal lines in Fig. 10(b) represent the constant frequencies of 5.6 GHz and 6.8 GHz. It can be observed in part (b) that frequency of 5.6 GHz corresponds to the LSR bandgap in the backward direction, while it corresponds to the second surface band of the bare substrate in the forward direction. Therefore, we expect a nonreciprocal behavior for f=5.6 GHz, so that the forward transmission is allowed and the backward transmission is forbidden. In contrary, frequency of 6.8 GHz corresponds to the sagittal surface band for the forward direction, while it corresponds to the LSR bandgap in the backward direction. Therefore, we expect a reciprocal, but highly attenuated transmission behavior for both the forward and backward excitations, when we apply a shear polarized source. Figures 10(c) and 10(d) depict the calculated iso-frequency contours for the low frequency surface coupled bands of the bandstructure, wherein cyan zones represent the bulk modes. Figure 10(c) displays the iso-frequency contours for frequencies lower than about 5.6 GHz and confirms the nonreciprocal behavior of the the left PnC structure at f=5.6 GHz. It can be observed that the iso-frequency contour of f=5.6 GHz indicates a complete anisotropic behavior, concerning the forward (k_y=0) and backward (k_x=k_y) directions, which leads to allowed transmission for forward incidence, and forbidden transmission for backward incidence. Figure 10(d) displays the iso-frequency contours for frequencies higher than about 6.5 GHz, wherein we can observe a sagittal and isotropic contour for f=6.8 GHz, denoting a nearly equal elastic wave velocity in all directions. Moreover, the inset in Fig. 10(d) shows the magnified view of the dashed rectangle zone in this figure, wherein we can observe the allowed transmission for surface coupled modes in Γ*X* direction (k_y=0). However, the inset clarifies that the backward surface excitation converts to the bulk modes (enters the cyan zone branch) for Γ*M* incident direction (k_x=k_y).

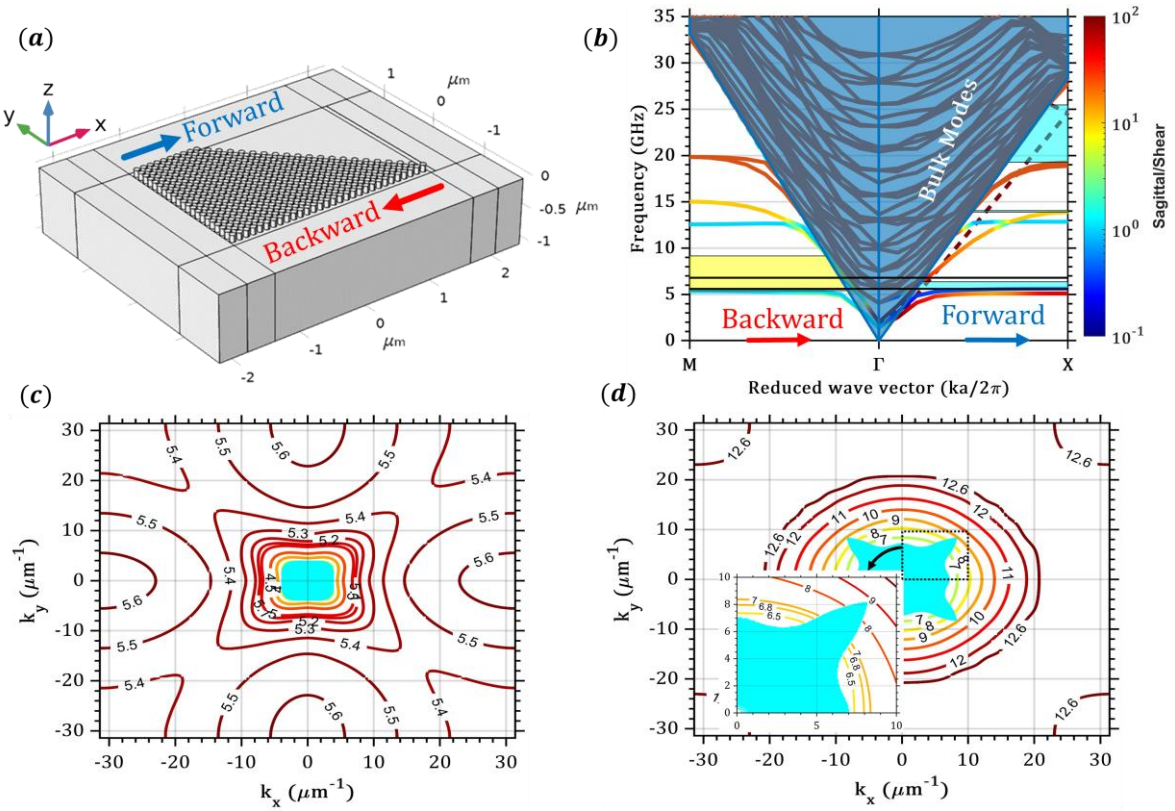

FIG. 10. (a) The individual left PnC, and (b) the relating band structure. (c, d) The iso-frequency contours around the second and the third bands.

Then, we present the calculated forward and backward transmissions of the left PnC for the shear polarized excitation in Fig. 11(a), which confirms the previous discussions based on the relating bandstructure (Fig. 10(b)). As shown, we achieve a maximum nonreciprocity of +14.8 dB at f=5.6 GHz, with the maximum forward transmission of -12.89 dB. The other worthy point that should be noted, is that the backward incident wave first enters the right PnC in the proposed complete device structure (Fig. 5), then enters the left PnC. On the other hand, we discussed in Fig. 7 that the backward shear polarized incident wave converts into a sagittal wave at f=6.8 GHz, during passing through the right PnC. Thus, we should consider the sagittal polarized excitation source for the left PnC, to elaborate the backward shear transmission behavior of the total structure with the PnC heterojunction at this frequency. Regarding this, in Fig. 11(b) we plot the calcuated shear incident forward transmission, superimposed with the sagittal polarized backward transmission of the individual left PnC. It can be observed that for frequencies above 5.6 GHz, the individual left PnC start the nonreciprocal behavior, so that the nonreciprocity approaches -11.7 dB at f=6.8 GHz. The data present in Fig. 11(b) helps to better explain the

transmission behavior of the total heterojunction PnC structure. Considering the numerical investigations of the individual right and left PnCs at *f*=6.8 GHz (during figures 6-11), we conclude that the shear polarized forward incident (as shown in Fig. 5) to the complete heterojunction structure, first passes through the left PnC, then couples to the right PnC and passes without significant polarization conversion, but shows considerable attenuation. However, the shear polarized backward incident to the complete heterostructre, first converts into sagittal mode during passing through the right PnC, then succesfully passes through the left PnC, while it shows a significant backward transmission. In other words, we observe a high backward transmission as compared with the forward transmission at *f*=6.8 GHz, the nonreciprocal behavior which is amplified when the left and right PnCs come beside each other and form the proposed heterostructure.

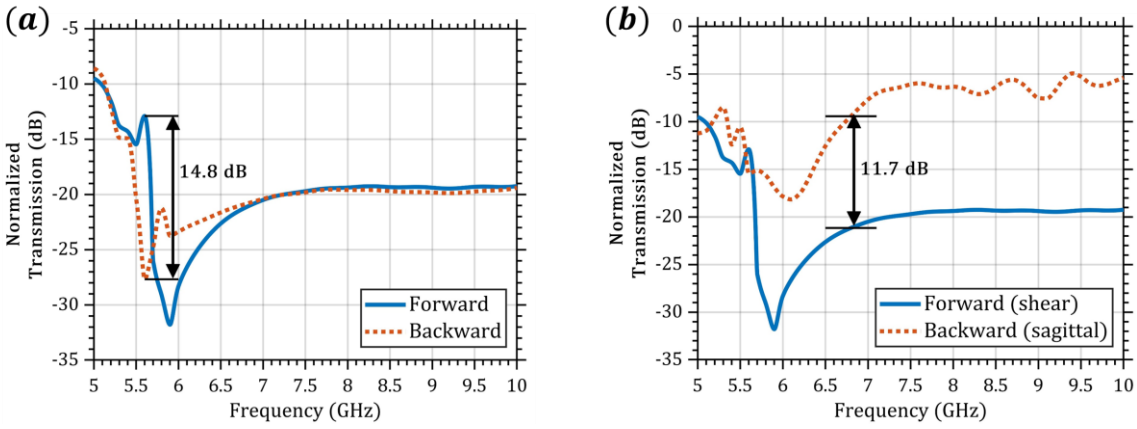

FIG. 11. The normalized transmissions in the left PnC for (a) the forward and backward of the shear polarized input, and (b) the forward/backward for the shear/sagittal polarized input.

Figure 12 shows the total displacement distribution for the individual left PnC at the nonreciprocal frequency of 5.6 GHz (parts (a), and (b)), besides two other reciprocal frequencies of 6.8 and 11 GHz (parts (c)-(f)). All displacements are demonstrated in the cross section view of the left PnC structure (*xz* plane) and are relating to the shear mode input. As shown in this figure, the incident elastic wave transmits through the left PnC by surface coupled resonances with the pillars, which are apparently observable for for the forward transmission at *f*=5.6 GHz. However, the backward incident at *f*=5.6 GHz remains confined to the pillars resonances, so that a small portion of elastic wave is transmitted to the output cutline, leading to a nonreciprocal behavior. At *f*=6.8 GHz, it can be

seen in Fig. 12(b) that the forward incident wave leads to resonances in pillars and decay along the *x* direction, coming decoupled from the surface elastic modes. However, for the backward incident, despite of the resonances in pillars, the elastic wave is mostly coupled to the bulk, as can be observed in part (d), so that no significant nonreciprocity is achieved here. For higher frequencies, such as 11 GHz, no elastic localization is observed in the pillars, and the energy is transmitted through out the whole cross section with a reciprocal behavior.

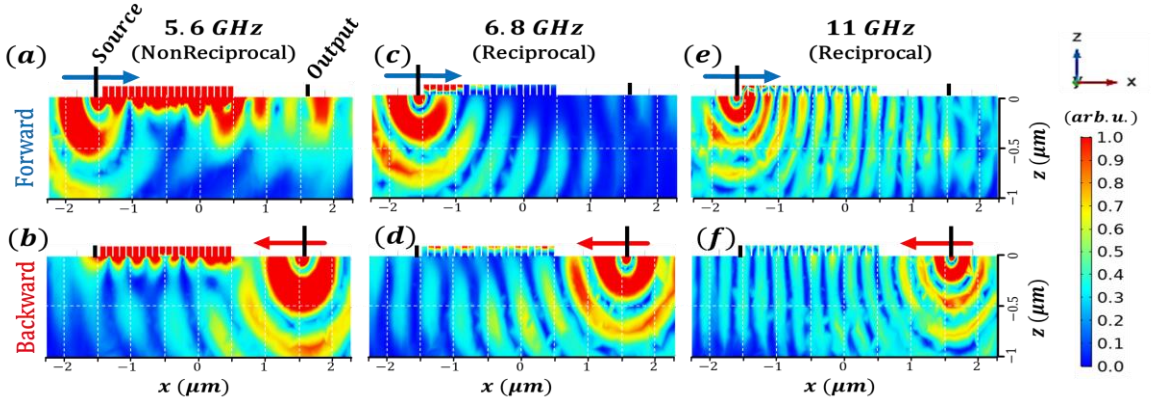

FIG. 12. Total displacement profiles of the individual left PnC in *xz* plane for the forward and backward incident directions at the frequency of (a, b) 5.6 GHz, (c, d) 6.8 GHz, and (e, f) 11 GHz.

Considering the aforementioned results regarding the transmission behaviors of the individual right and left PnCs, a significant nonreciprocal behavior is expectable for the complete proposed heterostructure device at f=6.8 GHz. Figure 13(a) shows the calculated spectrum of the nonreciprocity factor (NRF (dB)=10log(Backward Transmission/Forward Transmission)), versus the number of extended pillars (N_{ext}) in the proposed heterostructure device, when the interspacing gap is d=0. As it is shown, a significant NRF is achieved at f=6.8 GHz, and it is enhanced for N_{ext}>3, due to the hindered direct coupling between the incident excitation and the output port. NRF is maximized for N_{ext} =5, meaning that 5 extended pillars are adequate for blocking direct elastic coupling between the input incident and the output cutline. Hence, we assume N_{ext}=5 for the rest of our simulations. Figure 13(b), shows the forward and backward transmissions of the proposed heterostructure with N_{ext}=5 and d=0, confirming a significant NRF=31 dB, with an acceptable backward insertion loss of about 12 dB, at f=6.8 GHz. This significant SAW nonreciprocity at 6.8 GHz is mainly achieved due to three factors in the presented PnC heterostructure: (i) the difference between the surface coupled bands of the two

PnCs, originating from different pillar radii and lattice constants, and the heterojunction interface that leads to different elastic coupling strength in the forward/backward directions; (ii) The allowed coupling between the surface coupled modes of the PnC and the surface modes of the bare substrate; (iii) The allowed polarization conversion in the right PnC from shear to sagittal polarization for the backward incident, leading to excitation of the left PnC with a sagittal mode.

After the discussed band structure engineering, we investigate the effect of the gap space between the left and right PnCs at the heterojunction on the nonreciprocal behavior of the structure. Inserting a gap space (d), as shown in Fig. 5(b), the SAW coupling between two PnCs and the achieved NRF can be changed, consequently. The gap space (d) is defined as the distance between two adjacent unit cells along x direction, and is investigated from a_L to $6a_L$. Figure 13(c), shows the calculated maximum NRF value versus the normalized gap space (d/a_L), wherein a maximum nonreciprocity of about 34 dB is achieved for $d=2a_L$. It is notable that the NRF peak frequency is slightly shifted from 6.8 GHz (for $d= 0$) to 6.9 GHz (for $d=2a_L$) in the complete heterostructure, which is attributed to the modified elastic coupling and acoustic impedances relating to the PnCs. In Fig. 13(c) we have also displayed the gap space values normalized to the elastic wavelength (λ) at the top secondary x-axis. The forward and backward transmission values at the maximum NRF point are depicted in Fig. 13(d), versus varying d. As it is shown, the gap space value shows sinusoidal-like effects on the forward and backward transmission values. Fig. 13(d) shows that increasing d from zero to a_L or $2a_L$ even leads to increasing the backward transmission value from -12 dB to -9 dB or -10.68 dB, respectively. Therefore, it is observable that acoustic impedance modulation by varying gap space in the lattice constant range can also lead to a decreased insertion loss.

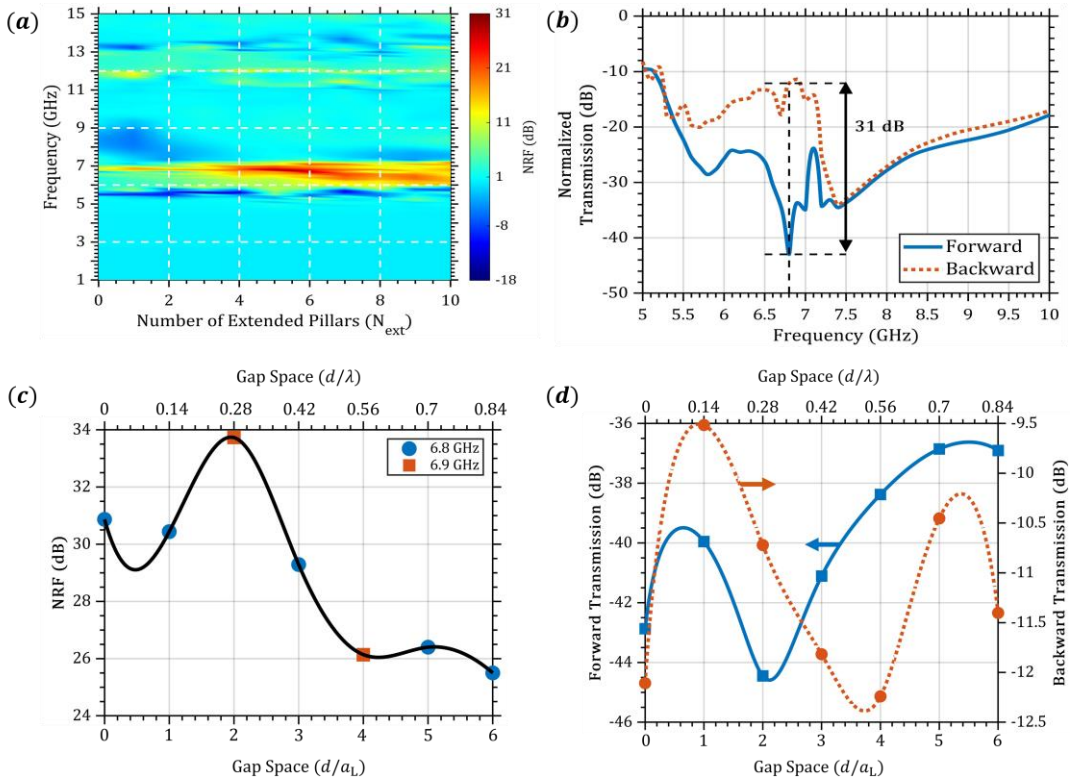

FIG. 13. Simulation results of the proposed device: (a) Spectrum of the calculated NRF versus varying N_{ext} for d=0. (b) The forward and backward transmission spectra with N_{ext} =5 and d=0. (c) Variation of the calculated NRF versus d value. (d) The forward and backward transmission values versus d.

The gap space effect can be further investigated by the elastic wave distriburion, as shown in Fig. 14. Figures 14(a-c), (d-f), and (g-i) are relating to the proposed heterostructure with different gap spaces equal to $2a_L$, $6a_L$ and $20a_L$, at the excitattion frequency of maxmimum NRF. Parts (b, e, h) in this figure indicate the top view schemes (xy plane), while the presented elastic wave distributions are related to the forward (left parts) and backward (right parts) excitations in the xz cross sections along the red dashed lines in the top view schemes (middle parts). For the forward excitations in this figure, it is shown that the elastic wave decouples from the surface after propagating through the left PnC. However, higher d values can lead to slightly enhanced surface coupling of the forward elastic wave. For the backward excitations, the elastic energy is localized inside the gap space between two PnCs, for smaller d values. However, this confinement is decreased for higher d values, and more elastic energy dissipates in the bulk substrate.

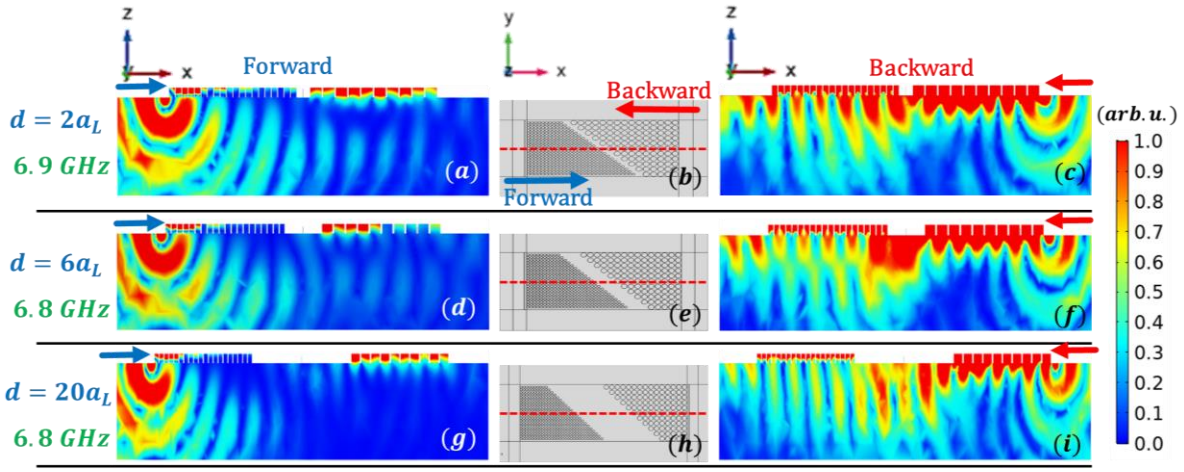

FIG. 14. The forward displacement, the top view scheme, and the backward displacement for (a, b, c) d=2a_L at 6.9 GHz, (d, e, f) d=6a_L at 6.8 GHz, and (g, h, i) d=20a_L at 6.8 GHz.

Hence, after optimizing the gap space value to achieve the maximum NRF value beside the maximum backward transmission value, we assume d=2a_L. Table I presents the final structral parameters of the optimized heterostructure device. As stated before, we assumed the same pillar heights in the left, and right PnCs all over the simulations, so that the propsoed heterostructure device can be fabricated without involving fabrication complexities or extra costs. Figure 15 indicates the calculated final forward/backward SAW shear transmission spectra for the proposed optimized heterostructure at f=6.9 GHz, wherein NRF=34 dB, and the backward transmission value equals -10.68 dB. Table II summarizes the output results of the proposed optimized nonreciprocal SAW device, as compared with other recent reports on nonreciprocal SAW devices. According to Table II, our proposed device is entitled as a promising candidate for SAW on-chip rectifier, because of both a high non-reciprocity factor, and a low insertion loss. Our device benefits from a simple fabrication process and does not need any external excitation for the achieved desired operation.

TABLE I. The parameters of the optimized heterostructure design to achieve the highest NRF and transmission values.

Parameter	Symbol	
Pillar radius of the left PnC	r_L	40 nm
Pillar radius of the right PnC	r_R	85 nm
Lattice constant of the left PnC	a_L	100 nm
Lattice constant of the right PnC	a_R	200 nm

Pillars height	h_p	100 nm
Number of extended pillars	N_{ext}	5
Gap space	d	$2\times a_L$= 200 nm
Substrate thickness	h_s	1 μm

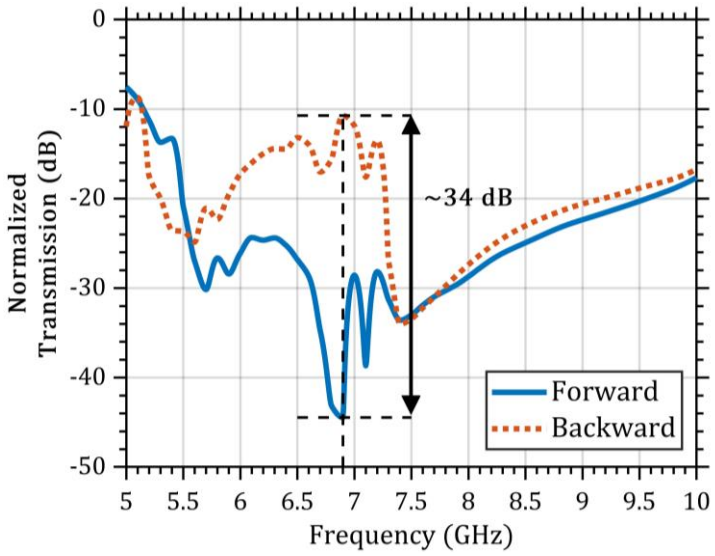

FIG. 15. The forward and backward transmission spectra in the designed nonreciprocal device with structural parameters, listed in Table I.

TABLE II. The output parameters of the optimized heterostructure device, as compared with the prevoius nonreciprocal SAW reports.

Reference	**Frequency**	**External excitation**	**NRF**	**Insersion loss (dB)**
[5]	GHz	Magnetic	20 %	-
[20]	GHz	Magnetic	45 dB	20
[21]	MHz	Electrical	2.5 dB	40
Our work	GHz	WO external excitation	34 dB	10.68

V. CONCLUSION

In summary, we proposed a static nonreciprocal SAW device based on a heterojunction in PnCs in GHz frequency range. In this structure, two PnCs with different pillar radii and lattice constants are coupled at a heterojunction interface. The initial design is based on the engineered band structures, and the sagittal to shear mode conversion. Our simulation results showed that a nonreciprocity as high as 34 dB is achieved in the proposed device with the

transmission of -10.68 dB at f=6.9 GHz for shear polarized excitation. This high nonreciprocal behavior is mainly attributed to the different response of PnCs to different incident directions and the polarization conversion that occurred in the PnC with a higher pillar radius. Moreover, by making an interspacing gap between the PnCs at the interface, it is shown that the elastic coupling strength between two PnCs are changed, so that both nonreciprocity and transmission values can be enhanced. The proposed nonreciprocal SAW device benefits from a simple fabrication process, without the need for external excitation fields for nonreciprocal behavior, which is suitable for on-chip miniature signal processing devices in wireless communication applications.

AKNOWLEDGEMENT

The authors acknowledge the financial support from Tarbiat Modares University through Grant #IG-39703.

Disclosures

The authors declare no conflicts of interest.

REFERENCES

[1] C. Caloz, A. Alù, S. Tretyakov, D. Sounas, K. Achouri, and Z.-L. Deck-Léger, Physical Review Applied **10**, 047001 (2018).
[2] H. Ren and Y. Xie, IEEE Transactions on Electron Devices **67**, 5144 (2020).
[3] X. Zhou, S. K. Gupta, X. Zhu, G. Su, P. Zhan, Y. Liu, Z. Chen, M. Lu, and Z. Wang, Physical Review Applied **13**, 044037 (2020).
[4] A. Cicek, O. Adem Kaya, and B. Ulug, Applied Physics Letters **100**, 111905 (2012).
[5] A. Hernández-Mínguez, F. Macià, J. M. Hernàndez, J. Herfort, and P. V. Santos, Physical Review Applied **13**, 044018 (2020).
[6] L. Shao, W. Mao, S. Maity, N. Sinclair, Y. Hu, L. Yang, and M. Lončar, Nature Electronics **3**, 267 (2020).
[7] M. Xu *et al.*, Science advances **6**, eabb1724 (2020).
[8] B. J. Chapman *et al.*, Physical Review X **7**, 041043 (2017).
[9] R. Lu, T. Manzaneque, Y. Yang, L. Gao, A. Gao, and S. Gong, IEEE Transactions on Microwave Theory and Techniques **67**, 1516 (2019).
[10] D. P. Morgan, International journal of high speed electronics and systems **10**, 553 (2000).
[11] P. Delsing *et al.*, Journal of Physics D: Applied Physics **52**, 353001 (2019).
[12] I. Group, IEEE 5G and Beyond Technology Roadmap White Paper, 2017.
[13] A. Winkler, R. Brünig, C. Faust, R. Weser, and H. Schmidt, Sensors and Actuators A: Physical **247**, 259 (2016).

[14] M. Mahmoud, A. Mahmoud, L. Cai, M. Khan, T. Mukherjee, J. Bain, and G. Piazza, Optics express **26**, 25060 (2018).
[15] C. Wang, C. Wang, D. Jin, Y. Yu, F. Yang, Y. Zhang, Q. Yao, and G.-J. Zhang, ACS sensors **5**, 362 (2020).
[16] D. A. Golter, T. Oo, M. Amezcua, K. A. Stewart, and H. Wang, Physical review letters **116**, 143602 (2016).
[17] M. M. Mehrnegar, S. Darbari, H. Ramezani, and M. K. Moravvej-Farshi, Journal of Lightwave Technology **37**, 2126 (2019).
[18] F. Taleb, S. Darbari, and A. Khelif, Journal of Applied Physics **129**, 024901 (2021).
[19] F. Taleb, S. Darbari, A. Khelif, and H. Taleb, Journal of Physics D: Applied Physics **54**, 225301 (2021).
[20] R. Verba, I. Lisenkov, I. Krivorotov, V. Tiberkevich, and A. Slavin, Physical Review Applied **9**, 064014 (2018).
[21] H. Zhu and M. Rais-Zadeh, IEEE Electron Device Letters **38**, 802 (2017).
[22] F. Taleb and S. Darbari, Physical Review Applied **11**, 024030 (2019).
[23] J. Babaki and F. Nazari, Journal of Physics D: Applied Physics **53**, 375301 (2020).
[24] S. E. Zaki, A. Mehaney, H. M. Hassanein, and A. H. Aly, Scientific Reports **10**, 1 (2020).
[25] M. Sledzinska, B. Graczykowski, J. Maire, E. Chavez-Angel, C. M. Sotomayor-Torres, and F. Alzina, Advanced Functional Materials **30**, 1904434 (2020).
[26] T.-G. Lee, S.-H. Jo, H. M. Seung, S.-W. Kim, E.-J. Kim, B. D. Youn, S. Nahm, and M. Kim, Nano Energy **78**, 105226 (2020).
[27] M. Javadi, A. Heidari, and S. Darbari, Current Applied Physics **18**, 361 (2018).
[28] A. Shakeri, S. Darbari, and M. Moravvej-Farshi, Ultrasonics **92**, 8 (2019).
[29] A. Khelif, Y. Achaoui, S. Benchabane, V. Laude, and B. Aoubiza, Physical Review B **81**, 214303 (2010).
[30] Y. Achaoui, A. Khelif, S. Benchabane, L. Robert, and V. Laude, Physical Review B **83**, 104201 (2011).
[31] Y. Chen, F. Meng, G. Sun, G. Li, and X. Huang, Journal of Sound and Vibration **410**, 103 (2017).
[32] Y. Guo, M. Schubert, and T. Dekorsy, Journal of Applied Physics **119**, 124302 (2016).
[33] F. Gao, A. Bermak, S. Benchabane, M. Raschetti, and A. Khelif, arXiv preprint arXiv:2012.15314 (2020).